Exploration of Ceramic Dielectrics for Microscale Dielectric Barrier Discharge Plasma Actuators

Justin C. Zito[1] and David P. Arnold[2]
Interdisciplinary Microsystems Group, Dept. of Electrical and Computer Engineering, University of Florida, Gainesville, FL, 32611, USA

Ryan J. Durscher[3] and Subrata Roy[4]
Applied Physics Research Group, Dept. of Mechanical and Aerospace Engineering, University of Florida, Gainesville, FL, 32611, USA

Microscale dielectric barrier discharge plasma actuators have been fabricated and experimentally characterized utilizing silicon dioxide for the dielectric barrier with thicknesses of 5 and 10 μm. Using a ceramic dielectric material provides improved device reliability by increasing the lifetime of microscale DBD actuators. Power, velocity, and thrust/force data are reported for several device geometries. The plasma net body force is computed by integrating the spatial body force, and the actuator's thrust is found using a control volume analysis. By estimating the wall shear force, the plasma force may be recovered for comparison. These two methods show good agreement in estimating the plasma body force.

Nomenclature

C	=	capacitance
f_{plasma}	=	spatial plasma body force
F_{plasma}	=	integrated/net plasma body force
f_{shear}	=	spatial viscous shear force
F_{shear}	=	integrated/net viscous shear force
I	=	current
n	=	number of periods
N	=	number of samples
μ	=	dynamic viscosity
P_{avg}	=	average power
Q	=	electrical charge
ρ	=	air density
T	=	net thrust
u	=	velocity component
V	=	voltage
Subscript		
x,y,z	=	streamwise, surface normal, and spanwise directions

[1] Graduate Research Assistant, Electrical and Computer Engineering, 216 Larsen Hall, Gainesville, FL 32611, Student Member AIAA.
[2] Associate Professor, Electrical and Computer Engineering, 213 Larsen Hall, Gainesville, FL 32611, Member AIAA.
[3] Research Mechanical Engineer, Air Force Research Laboratory, Wright-Patterson Air Force Base, Ohio 45433, Member AIAA.
[4] Associate Professor, Mechanical and Aerospace Engineering, 336 MAE-B Bldg., Gainesville, FL 32611, Associate Fellow AIAA.

I. Introduction

TYPICALLY consisting of two electrodes (one exposed and one insulated) separated by a dielectric material, the dielectric barrier discharge, or DBD, is capable of generating a weakly ionized, non-thermal plasma upon the application of a high voltage differential across the two electrodes. The self-limiting nature of the discharge allows DBD's to operate at moderate pressures without transitioning to an arc[1]. As such, the DBD has seen substantial attention over the last couple of decades with numerous uses being explored. Applications include biological and waste sterilization, visual display panels, material surface treatments, and active flow control. In reference to the later, as fluidic actuators, the discharge couples with the surrounding neutrally charged medium, typically air, imparting/inducing a body force on the fluid. This coupling is a result of collisional exchanges between neutrals and ionized particles whose motion in governed by a Lorenztian force. As an actuator, the DBD is capable of locally injecting momentum to a flow without the need of moving parts or substantial modifications to the aerodynamic surface. A nearly instantaneous response time is guaranteed by the purely electrical device.

Although the DBD actuator construction is fairly straight-forward, dimensional control and alignment are limited by the manual hand-assembly of the actuator. Recently, DBD actuators have been fabricated and characterized having microscale dimensions and showed promising performance metrics[2]. The microscale actuators are capable of inducing velocities of 2 m/s and demonstrated up to 3 mN/m of thrust force. These actuators were manufactured using a 10-µm-thick polyimide layer for the dielectric barrier.

In this work, the actuators are fabricated with silicon dioxide (SiO_2) for the barrier layer with thickness of 5 and 10 µm. The devices are manufactured using semiconductor processing techniques to enable microscale dimensions with accurate dimensional control and alignment. The silicon dioxide layer is deposited using plasma-enhanced chemical vapor deposition (PECVD) and allows for accurate thickness control. Figure 1 shows a microscale DBD actuator during discharge as well as a cross-section schematic indicating the actuator geometry[2]. The powered electrode and electrode gap are kept constant in these experiments, while the dielectric thickness and ground electrode widths are varied. The different device geometries are referred to by their ground electrode size.

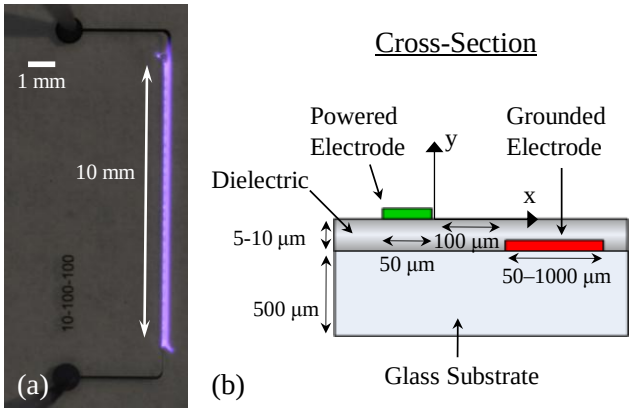

Figure 1. Top view of microscale DBD actuator shown during discharge (a), and a cross-section schematic view (b)[2].

II. Fabrication

Figure 2 illustrates the fabrication process for the microscale DBD actuators, showing cross-section schematics of each step. First, the bottom electrode is patterned using photolithography techniques and the electrode is sputter deposited onto the glass substrate (Fig. 2a). The electrodes are made of 500-nm-thick copper over a 50-nm-thick titanium layer to promote adhesion between the copper and glass. Next, the silicon dioxide dielectric layer is deposited using PECVD (Fig. 2b). The silicon dioxide is then patterned and dry etched to allow for contacts with the bottom layer of electrodes (Fig. 2c). A photoresist etch mask is used to protect the areas of the dielectric that are not to be etched. The etching process is performed using a reactive ion etch (RIE) process, and the photoresist layer is removed using solvents after completing the etch. Finally the top electrode is patterned and deposited in the same fashion as the bottom electrodes (Fig. 2d). Further details on these fabrication process steps can be found in any general text on semiconductor manufacturing technologies.

After completing the device manufacturing, measurements are made to verify the dielectric layer thickness as deposited by PECVD. A profilometer is used to make a one dimensional line scan across the device topology. The profilometer is a Dektak (model 150) diamond-tipped stylus profilometer with sub-nanometer resolution. The tip of

the stylus is 12 μm in diameter and applies 10 mg of force as it scans along the dielectric surface. The profile shown in Fig. 3 corresponds to a scan across an etched region in the dielectric to provide an opening to the lower electrode for electrical contacts. The scan verifies that the 10 μm target thickness was achieved.

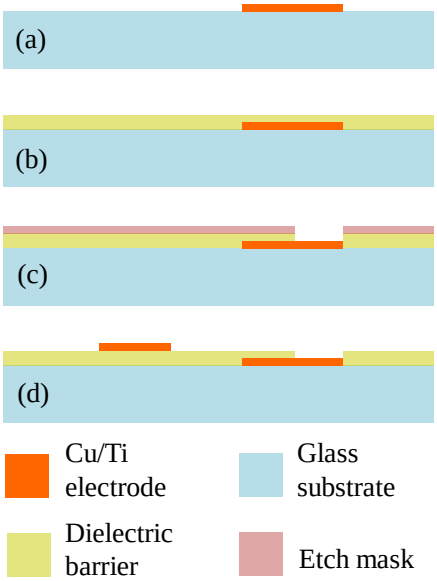

Figure 2. Fabrication process steps.

As mentioned previously, the first generation of microscale DBD actuators were made utilizing polyimide for the dielectric barrier. However, breakdown consistently occurs within as little as seconds to a few minutes of operation; as soon as the dielectric layer fails there becomes an effective short circuit causing a current surge and the dielectric is subsequently charred from joule heating. It was found that the primary failure mechanism is due to electrical breakdown of the polymer layer caused by etching/erosion of the film (due to the discharge process). A simple failure analysis was performed on the polymer devices to investigate the cause of dielectric failure as shown in Fig. 4. Figures 4a and 4b show an optical image of the device before and after it has failed. Figure 4c provides an SEM image of the dielectric surface in the region where the discharge has occurred.

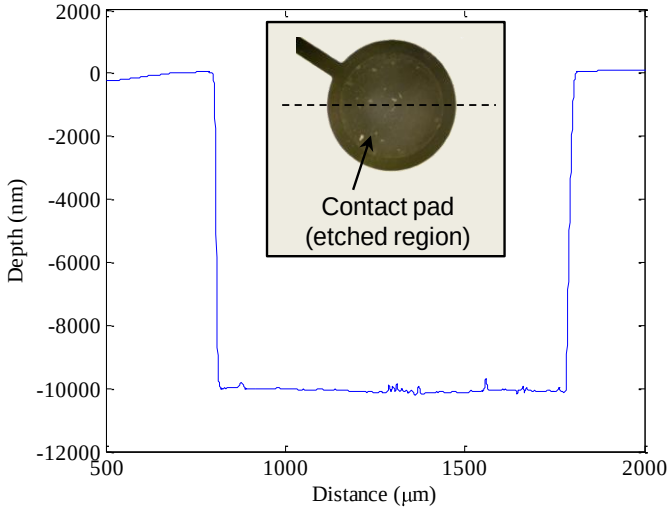

Figure 3. Profilometer measurement of SiO_2 dielectric layer topology, scanned over bottom electrode contact pad (see insert) for device with a target dielectric thickness of 10 μm.

There is noticeable erosion of the polyimide, especially near the front edge of the anode from where the discharge originates. This erosion is due to the collisional processes that sustain the discharge, which constantly bombard the dielectric surface causing material to sputter from the surface. Eventually, the polymer develops 'pits' or regions of deep erosion, and shortly after one of these regions punches entirely through the dielectric, creating a

low resistance path for current to travel. The failed region is magnified in Fig. 4d; the polymer around the point of failure becomes charred due to the increase in current which occurs almost instantly after the barrier fails.

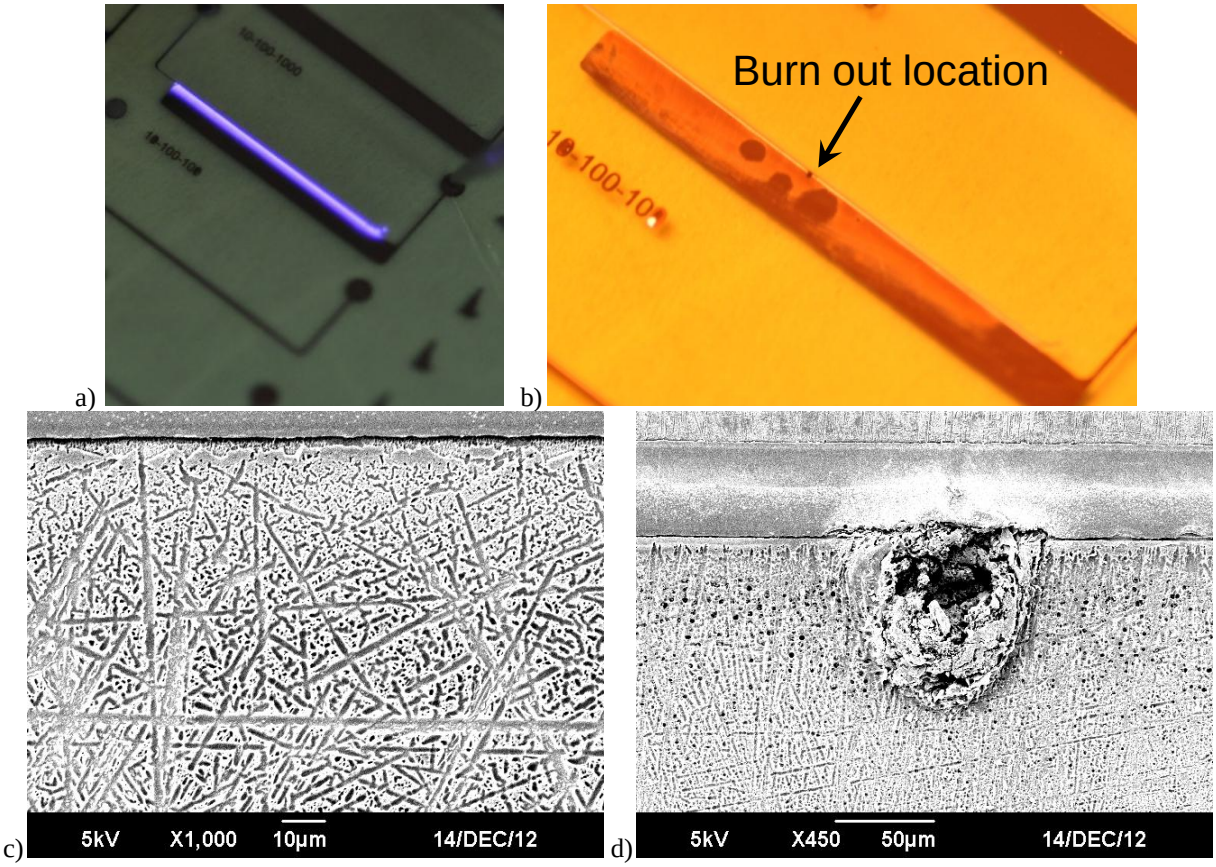

Figure 4. Polyimide failure analysis a) device in operation, b) device after burning out, c) SEM image of polyimide surface in discharge region (anode edge shown horizontal across top of image), d) SEM image of burn out region.

By moving away from organic polymer-based dielectric materials we aim to improve the duration, and thus the reliability, of the microscale DBD actuators. Ceramic dielectric barriers (i.e., glass) have been successfully utilized in many DBD experiments over the last decade and demonstrate improved resilience over organic materials such as epoxies and polymers (e.g., Kapton® tape). The data reported in this work correspond to a new generation of microfabricated DBD actuators having silicon dioxide as the dielectric barrier.

III. Experimental Methods

Experimental characterization of microscale plasma devices is complicated by the fine spatial dimensions and short temporal scales of the fluidic response, as well as the small magnitude (nano- to micro-Newtons) of the mechanical force response. Accurate measurement of these quantities is of critical importance for improving fundamental understanding of the microscale physics, validating numerical models, and fueling new applications for these plasma devices. As such, characterization of microscale DBD actuators requires accurate data acquisition equipment along with maintaining sound engineering methods throughout the experimental setup and measurements collection. In order to use microscale DBD actuators for flow control applications, their electrical, fluid and mechanical performance first must be quantified and must also provide repeatable results with minimal variation between devices. The methods and equipment used for device characterization are presented in this section.

Figure 5 indicates the orientation of the actuator with respect to the coordinate axes. This orientation is used throughout the characterization of both velocity and force data. The x-direction corresponds to the streamwise flow, the z-direction to the spanwise flow, with the y-direction being normal to the actuator's surface.

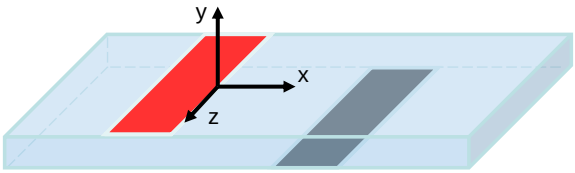

Figure 5. DBD device showing orientation of x,y,z coordinate axes.

A. Electrical Characterization

The electrical setup is shown in Figure 6. A sinusoidal input voltage (~kHz frequency) is synthesized by a function generator (Tektronix AFG 3022B). The voltage is then amplified to the kilovolts range using a high-voltage power amplifier (Trek model 30/20), which is connected directly to the DBD actuator terminals to create the plasma discharge.

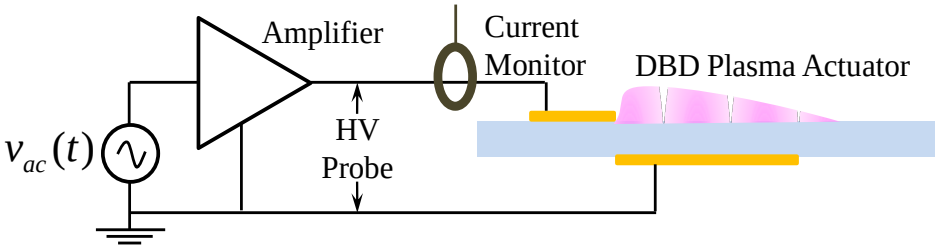

Figure 6. Schematic of typical power supply and electrical measurement probes for DBD plasma generation.

For the electrical characterization, both instantaneous and average electrical quantities are of interest. The voltage across the device terminals is measured using a high-voltage probe (Tektronix P6015A), and the current entering the device is measured with an inductive coil current monitor (Pearson 2100). A digitizing oscilloscope (Tektronix DPO3014) captures both of these signals, capable of sampling rates up to 2 GSa/s (giga-samples per second) with a record length of 1 million points.

The time-average power consumption is computed by averaging the instantaneous power over an integer number of periods using MATLAB software. Using the discrete set of sampled data captured by the oscilloscope, the time-average power is found by averaging the voltage-current product over the total number of data samples, *N*, according to

$$P_{avg} = \frac{1}{N}\sum_{j=1}^{N}(V_j \times I_j). \tag{1}$$

Note that the number of samples, *N*, should correspond to an integer number of periods of data for Equation 1 to be valid.

1. *Alternative Power Measurement Methods*

The current can be monitored a variety of ways depending on the available equipment. An inductive coil is commonly used within the DBD research community to measure the alternating current flowing into the DBD actuator. Alternatively, a small resistor is sometimes used when a current monitor is not available. The resistor is placed in series between the DBD actuator and ground. The resistance is typically 100 Ohms or smaller such that the voltage drop across it is much smaller than that across the actuator load. This allows for a standard voltage probe (i.e., does not require a high-voltage probe) to measure the resistor voltage, and the current is then computed via Ohm's law.

The current signal is most challenging to resolve. Large spikes corresponding to conduction current are superimposed on an underlying sinusoidal component or displacement current signal. These current spikes can reach over two orders of magnitude in amplitude compared with the amplitude of the displacement current, which follows the periodic frequency of the AC input. In order to capture the large current spikes, the oscilloscope's vertical resolution must be set accordingly. This causes the sinusoidal component of the current to become compressed greatly and results in very poor resolution of the displacement current component. Inversely, if the resolution is set finer to better resolve the displacement current, the current spikes are clipped. An investigation of this tradeoff in the current signal resolution is presented in the following section.

Lissajous figures are used as an alternative method to compute the average power dissipated in a DBD[1,3-8]. Instead of plotting the voltage and current waveforms with respect to time, the signals are plotted against each other, creating a Lissajous figure. The resulting plot is elliptical-shaped in which the aspect ratio of the ellipse is related to the phase shift between the two signals. In this case a small capacitor, referred to as a measurement capacitor, is placed in series between the DBD actuators' cathode and ground. The measurement capacitor (~nF) is chosen to be a few orders of magnitude larger than the capacitance of the actuator (~pF) such that the load capacitance is dominated by the plasma device. The voltage across the capacitor is monitored and used to compute the charge accumulation Q on the capacitor, where $Q = CV$. The charge-voltage characteristic curve is integrated to find the average power. In this method, the voltage across the measurement capacitor is typically noisy following the conduction current spikes from the dielectric barrier discharge. To 'clean up' the signal, the voltage across the measurement capacitor is averaged while recording. The averaged signal is used in the integration of the average power, and suppresses many of the discharge events.

Ashpis et al.[7] implemented a non-linear compression circuit between the DBD actuator and ground. This circuit is used to suppress the large current spikes without attenuating the sinusoidal component in order to better resolve both the sinusoidal current as well as the current spikes simultaneously. In addition to the compression circuit, Ashpis et al.[7] provides a thorough overview and comparison of the different methods available for computing the power dissipated in a dielectric barrier discharge. The reader is referred to this reference for details in these power measurement methods. In addition, the electrical performance of DBD actuators is thoroughly investigated as reported by Kriegseis et al.[6] In this work, the power consumption is related to the capacitance of the discharge, the thrust force and also the streamwise extent of the plasma discharge region.

2. Considerations for Power Measurements

There are several nuances to consider when computing the power consumed for DBD actuators. These apply to both the micro- and macroscale. Variables such as the oscilloscope sampling rate, the current amplitude resolution, and the number of point or periods recorded can affect the average power value. As mentioned in the previous section, there is a trade-off in resolving the components of the current signal.

The current resolution is first investigated. A microscale actuator is tested (100 µm ground geometry, 10 µm thick silicon dioxide dielectric) at 3.5 kVpp and 1 kHz input, and 100 periods of the voltage and current waveforms are downloaded for each of three current resolution settings. The oscilloscope is set to 20, 50 and 100 mA/division for consecutive recordings (Fig. 7). The sequence of these three current resolutions is repeated four times, again recording 100 periods during each download and integrated to compute the average dissipated power.

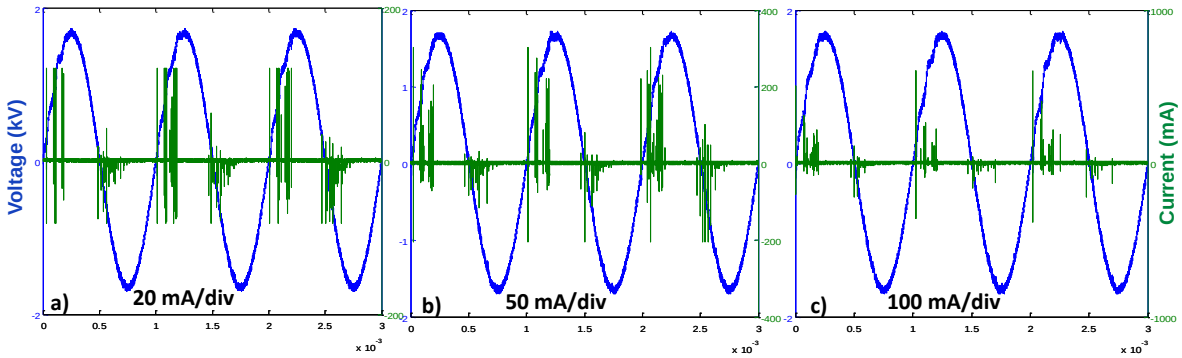

Figure 7. Voltage (blue) and current (green) waveforms plotted with time for different oscilloscope current resolution settings. Current channel set to a) 20 mA/div, b) 50 mA/div, and c) 100 mA/div.

The average power values corresponding to the waveforms in Fig. 7 are reported in Fig. 8. The average power increases when using a larger range, i.e., with decreased current resolution. The conduction current spikes are not clipped when using a larger dynamic range, and the large amplitudes of the current spikes are captured and contribute to the average power calculation. With increased resolution, the spikes are clipped more heavily and they do not contribute accurately in the average power calculation. The power values in blue circles correspond to the largest geometry actuator, and vary from 0.14 – 0.23 W, indicating that nearly half of the dissipated power is not captured when clipping the current in these data. Similar power data is reported in Fig. 8 for smaller device geometry (red diamonds). The smaller device consumes considerably less power, and the variation (percentage) between the power values based on the current resolution is even greater. The current spikes correspond to the discharge events, contributing to the conduction current which pertains to the real power consumed. The sinusoidal component represents the displacement current that travels back and forth in and out of the load, and pertains to the

reactive power due to the capacitance of the DBD actuator. While the sinusoidal component contributes some real power (amount depending on the phase between current and voltage), it is more important to capture the spikes in the current which contribute most to the real power dissipated in the DBD.

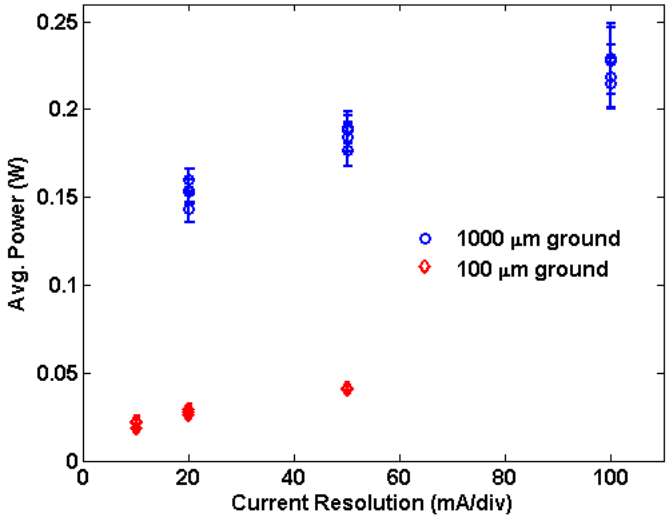

Figure 8. Average power as a function of current waveform resolution for two microscale DBD actuator geometries. Both devices have a 5-μm-thick silicon dioxide dielectric and are operated at 3.5 kVpp, 1 kHz.

The following example is discussed to further clarify these effects. There are eight divisions over the vertical range of the oscilloscope, and there are 8 bits dedicated to the vertical resolution corresponding to 256 discrete amplitude levels. A typical value for the amplitude of the sinusoidal current component for the microscale actuator is ~1 mA. At 20 mA/division resolution, the current signal achieves $8*(20\text{mA})/2^8$ = 0.625 mA resolution. This corresponds to only three or four values for which the sinusoidal current will be discretized. In this case, there is poor resolution over the periodic component of the current, and the spikes will be clipped at +/- 80 mA. With increased current resolution, the displacement current may be better resolved at the cost of increased attenuation of the conduction current signal, resulting in misleading low power values.

The next variable investigated is the sampling rate, or time resolution, of the oscilloscope. This test was performed using a macroscale DBD actuator, having 5 mm wide copper strip electrodes and a 3 mm thick PMMA dielectric. The device was operated at 14 kHz and 1 million points were recorded. The sampling rate is varied from 5 MSa/s up to 250 MSa/s with eight total increments (5, 6.25, 8.33, 12.5, 25, 50 125 and 250), and the average power is computed for each case over an integer number of periods (depending on the sampling rate). The results are shown in Fig. 9 for five voltage input values. The average power has little dependency on the sampling rate, with a slight decrease in the power for the slowest sample rate (5 MSa/s). From 6.25 – 250 MSa/s the power values are consistent and independent of the sampling rate.

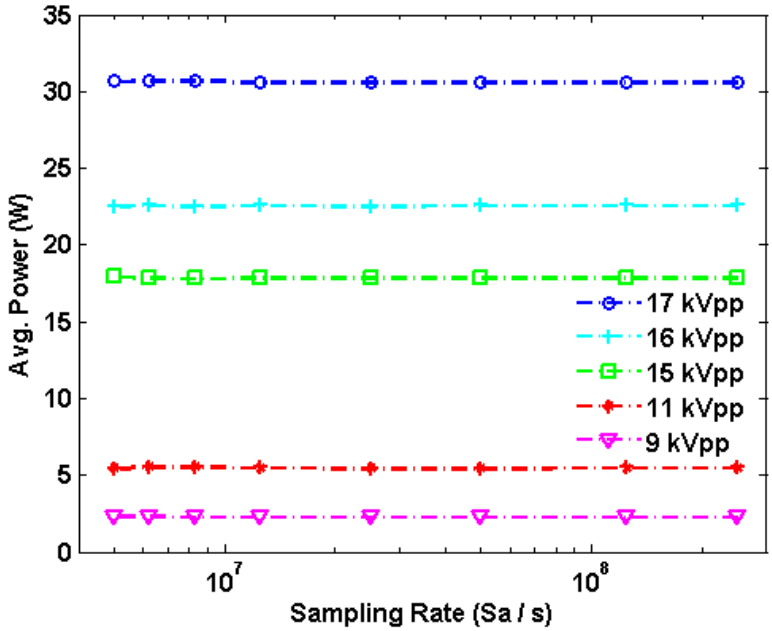

Figure 9. Average power as a function of sampling rate of a macroscale DBD actuator.

Instead of the sampling rate, the number of periods recorded is of more importance for an accurate power measurement. The same macroscale actuator was used for this experiment. The frequency was kept at 14 kHz and the sampling rate was set to 250 MSa/s, providing 56 periods of data for each recording. The data was segmented into individual periods and a running average was performed over the 56 periods.

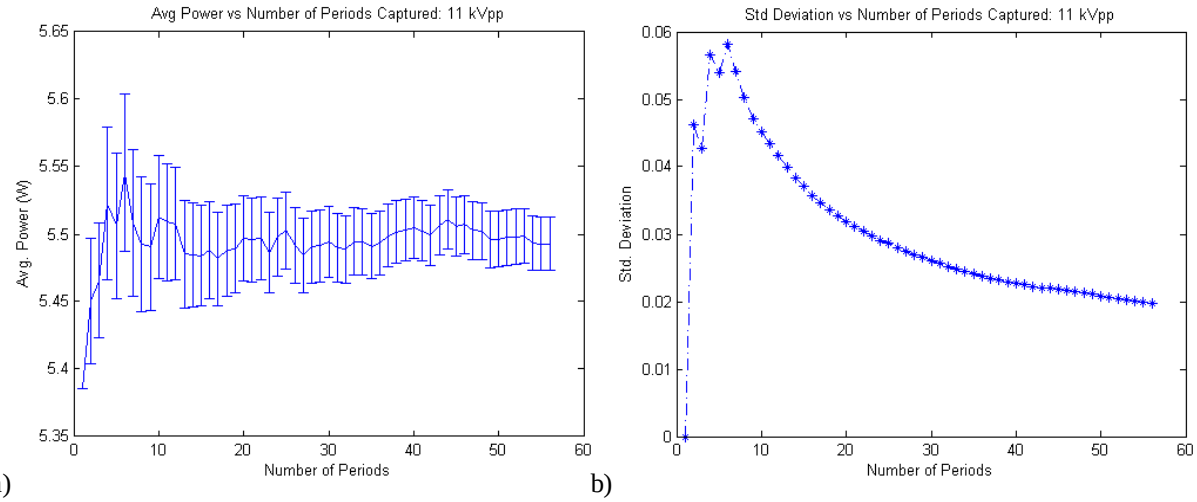

a) b)

Figure 10. a) Average power over *n* periods shown with standard deviation error-bars. b) Standard deviation of the average power over *n* periods.

Figure 10 plots the mean power as a function of the number of periods used for averaging. In Fig. 10a, the error-bars correspond to the standard deviation in the mean power value over *n* periods, while in Fig. 10b only the standard deviation is plotted over *n* periods. From these plots, over 10 periods are required before the mean power value begins to remain within its standard deviation. Acquiring even more periods reduces the standard deviation and provides more accurate average power data, with a tighter confidence interval.

To summarize, the mean power is affected most by the resolution of the current amplitude. A sufficient number of periods should be recorded and included in the mean power computation. The specific number of periods may vary based on the actuator geometry and electrical inputs, and so a running average analysis is recommended to ensure enough periods are captured. Finally, the sampling rate shows little influence on the power data, so long as the signals are sufficiently resolved in time. A low-end figure of merit for the sampling rate is to capture at least 500 points per period.

B. Fluidic Measurements

A spatial velocity map of the induced wall jet is of primary interest for fluidic characterization. Flow visualization techniques may be used qualitatively to view and compare the profile of the micro DBD induced flow with that of the macro DBDs. For quantitative velocity measurements, the fluid velocity may be measured using a number of methods. Non-intrusive test methods are preferred for two primary reasons; first, the large electric field for plasma discharge requires that no metal probes be used nearby, eliminating the possibility for utilizing hot wire velocimetry. Second, the induced velocity occurs in close proximity to the surface making it challenging to use physical probes without disturbing the flow. Non-metallic pitot or stagnation probes are a possible option, although they are limited in near-wall resolution due to restrictions in the probe diameter. A non-intrusive method, namely two-component particle imaging velocimetry (PIV), will be used to make the velocity measurements.

Two-component PIV measurements provide a two-dimensional cross-sectional image of the flow. A PIV image of the induced flow from a macroscale DBD actuator is illustrated in Fig. 11[9]. The vectors indicate the flow is being entrained near the upper electrode and pushed along the surface in the downstream direction, revealing the profile of the induced wall jet. Using a standard macro-lens in combination with typical optical teleconverters, an adjustable field of view (FOV) from ~20 – 60 millimeters (streamwise) may be obtained. When used with a high resolution CCD camera, it provides a spatially resolved detailed image of the induced flow for the DBD actuators. The profile of the flow field for microscale actuators follows as a scaled version of that observed with macroscale DBD actuators, where the maximum velocity occurs just above the dielectric surface.

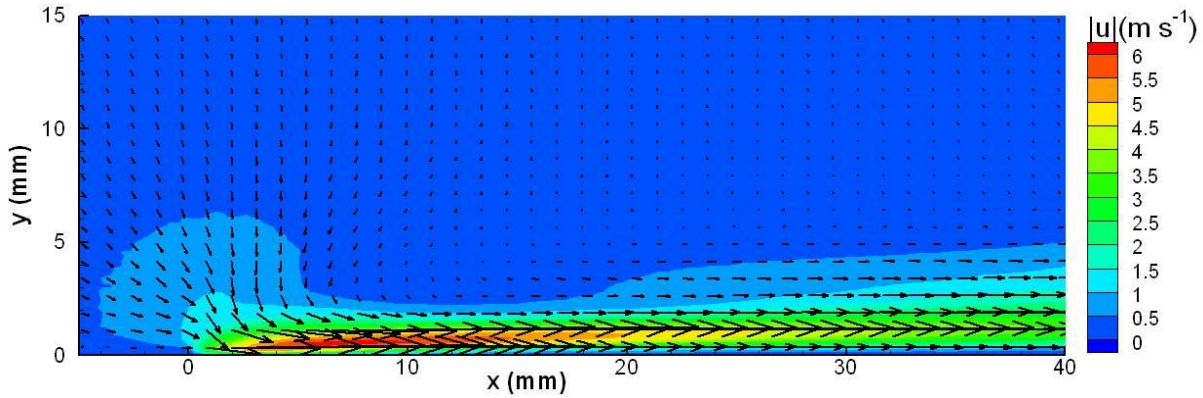

Figure 11. PIV data showing time averaged induced velocity flow field from a standard macroscale DBD plasma actuator[9].

The actuators are tested directly on the glass wafer substrate on which they were fabricated. A large acrylic chamber is used to prevent the induced flow from being affected by ambient fluctuations in the laboratory creating a quiescent test environment. The chamber is 0.61 m square by 1.22 m tall, and also helps to keep large amounts of ozone from circulating into the laboratory.

A dual cavity pulsed Nd:YAG laser (New Wave Research Solo PIV II 30) is used to generate a light sheet along the centerline of the actuator in the direction of the induced flow (normal to the span). In order to ensure that the laser sheet is centered and perpendicular to the device span, reference indicators were included in the fabrication design which allow the light sheet to be accurately aligned. The laser sheet is adjusted using attached, on-axis optics to achieve a 1 mm thick beam waist. The test area is seeded with flow tracing particles. Ondina oil is used for the seeding material, which is vaporized using a TSI atomizer (Model 9302) using 25 psi of pressure. Using these settings, the atomizer produces seed particles with a mean diameter of ~0.8 µm[10]. Durscher and Roy[9] previously showed reasonable agreement between PIV data obtained using ondina oil as the seeding material and pitot static measurements implying the ondina particles are negligibly affected by the electrostatic forces near the high-voltage electrodes.

For each PIV test, 300 image pairs are taken at a repetition rate of 7.2 Hz. The time between laser pulses (*dt)* is adjusted based on the induced velocity. The *dt* is set to maintain a particle displacement of 5 to 7 pixels between image pairs for optimal data correlation. A LaVision camera (ImagerPro X 4M, 2048 x 2048 pixels[2]) is used to capture the PIV images and is fitted with a 105 mm lens. In some cases a teleconverter lens (1.4x or 2x) is used in addition to the primary lens, reducing the FOV and increasing the spatial resolution.

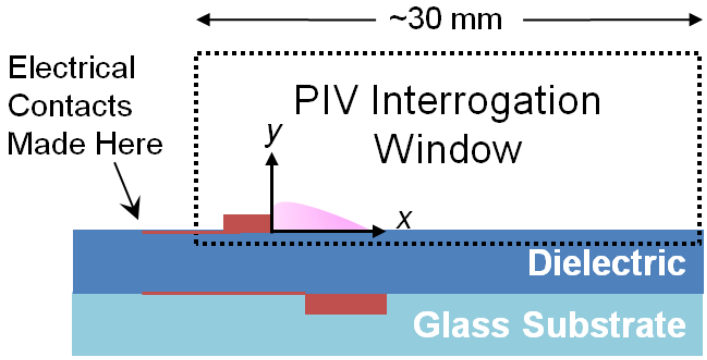

Figure 12. Schematic of experimental setup for velocity measurements indicating the field of view used with reference to the location of the electrical contact points.

LaVision's proprietary DaVis 7.2 PIV software package is used to capture, pre- and post-process the PIV images. Prior to data collection, image calibration is performed using a 40 mm square, two tier calibration plate. Data post-processing begins by computing the average intensity of each image frame. The average intensity is then subtracted from each raw image in order to increase the signal-to-noise ratio of the image. A particle intensity correction is applied locally over a window of 3 to 5 pixels allowing for smaller particles to be more effectively included in the image correlation[10]. The correlation is then applied using a multi-grid / multi-pass process. The first pass applied a 32 x 32 pixel window with 50 % overlap, followed by two refining passes using a 16 x 16 pixel window and 50 % overlap. The resulting velocity flow field has a vector resolution of 110 µm for a 30 mm wide x 20 mm high field of view, and ~220 µm for a larger field of view (46 mm x 25 mm).

The electrode's contact pads were designed so that they do not block the camera's field of view of the wall jet during the PIV measurements. The induced flow structure begins near the edge of the exposed electrode and extends

downstream, taken as the direction toward the grounded electrode (positive x direction). A schematic of the velocity measurement set up is provided in Fig. 12 indicating the location of the velocity interrogation window with respect to the electrical contacts.

The convergence of the time-averaged velocity is investigated in Fig. 13 in order to determine whether 300 images provide a statistically sufficient number of image pairs. The data in Fig. 13a displays the x-component of the velocity measured at x = 3 mm and y = 0.5 mm, and in Fig. 13b for x = 8 mm and y = 1.5 mm. These point are chosen to investigate the region in the core of the wall jet (x = 3 mm) and also the downstream diffused region of the induced flow (x = 8 mm). The velocity remains fairly constant at 3.0 and 3.5 kV_{pp} with fluctuations (standard deviation / average velocity) within 2.1 % of the mean velocity. At 4 kV_{pp}, the data at x = 3mm varies slightly more, within 2.4 % of the mean velocity value, although at x = 8 mm (Fig. 13b) the velocity variation is 1.3 %. The overall variation in the averaged velocity is within 3.0 % and permits confidence in the time-averaged velocity measurements.

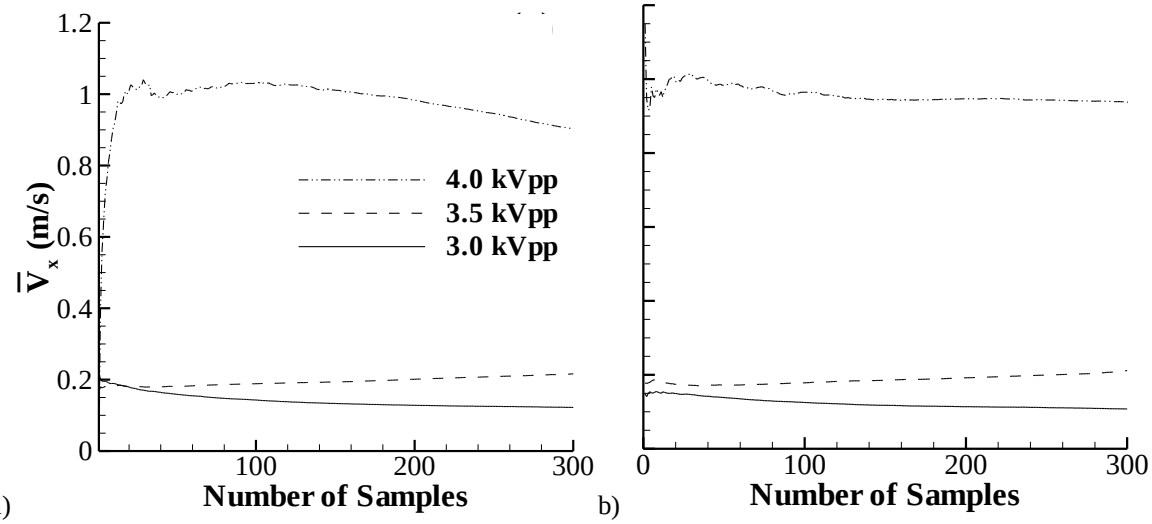

Figure 13. Velocity convergence plots over 300 image pairs for the x-component of velocity. a) x = 3.0 mm, y = 0.5 mm. b) x = 8.0 mm, y = 1.5 mm.

C. Mechanical Measurements

The mechanical response of a macroscale DBD actuator is typically characterized by its induced thrust[9,11-17]. Here the term thrust describes the net reaction of the actuator due to pressure, shearing, and plasma induced forces. The thrust produced by a macroscale DBD actuator, is typically on the order of 10's mN/m and can be measured directly by mounting the actuator on a digital force balance. The resolution of these balances typically ranges from 1 or 10 mg. However, for microscale DBD devices, the thrust is on the order of 0.1 – 1 mN/m [2]. For an electrode length of 10 mm, the measured thrust before normalizing to the electrode length is on the order of 1 – 10 μN (0.1 – 1 mg). Hence, the microscale DBD thrust is, at best, on the order of the balance's minimum detectable signal. For the smaller of the microscale DBD geometries (50 μm ground geometry), the thrust is even smaller and cannot be measured on a typical balance.

Instead of a direct measurement, the net reaction thrust and/or plasma induced body force may be inferred from the velocity field[4,9,15,16]. Two methods are investigated to do so: first, a control volume analysis is used to compute the net thrust based on the difference in momentum flux through a set of boundaries. The second method utilizes the Navier-Stokes equations to solve for the body force term spatially over all points within the velocity field. The total force may then be determined through

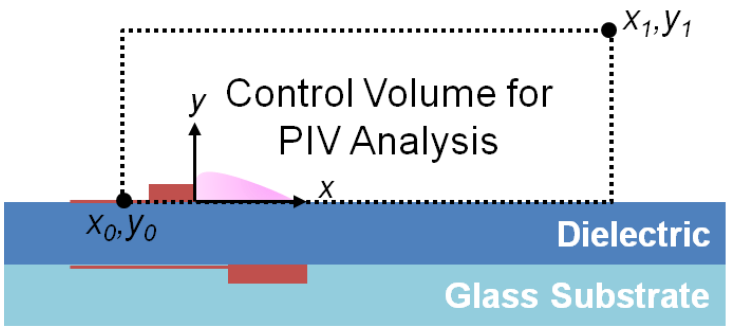

Figure 14. Schematic view of the control volume used for extraction of thrust data from PIV measurements.

integration. The details of these two methods follow.

1. Control Volume Analysis

In the first method, the thrust acting on the device may be estimated via a control volume (CV) analysis using the measured velocity data. Two recent publications[4,9] have compared control volume extracted thrusts with direct measurements obtained using a digital balance. The results showed relatively good agreement. As shown in Fig. 14, a rectangular control volume is applied to the flow field. The individual components of the thrust, T_x and T_y, are computed using the conservation of momentum equations, assuming two-dimensional flow (negligible spanwise variations), time independence (time-averaged data is used) and negligible pressure gradients (constant pressure). The analytical expression for the individual x and y force components follow, normalized by the electrode length (units of N/m):

$$T_x = F_{plasma,x} + F_{shear} = \int_{y_o}^{y_1}\int_{x_o}^{x_1} f_{plasma,x}(x,y)dxdy + \int_{x_o}^{x_1} f_{shear}(x,y_0)dx$$

$$= \rho\left[-\int_{y_o}^{y_1} u_x^2(x_o,y)dy + \int_{x_o}^{x_1} u_x(x,y_1)u_y(x,y_1)dx + \int_{y_o}^{y_1} u_x^2(x_1,y)dy \right] \tag{2a}$$

$$T_y = F_{plasma,y} = \int_{y_o}^{y_1}\int_{x_o}^{x_1} f_{plasma,y}(x,y)dxdy$$

$$= \rho\left[-\int_{y_o}^{y_1} u_x(x_o,y)u_y(x_o,y)dy + \int_{x_o}^{x_1} u_y^2(x,y_1)dx + \int_{y_o}^{y_1} u_x(x_1,y)u_y(x_1,y)dy \right] \tag{2b}$$

In the above equations, the density of air, ρ, is taken as 1.18 kg/m^3 corresponding to a temperature of 25 °C and is assumed spatially constant throughout the analysis. Constant density is assumed in similar works[4,9] and a formal investigation is presented by Enloe et al.[18], where a 2 % increase in the fluid density was observed 1 mm above the actuator surface near the exposed electrode edge.

To extract the thrust results from the PIV data, the integrals in Equations 2 are applied to the time averaged velocity data from the PIV measurements using MATLAB software. A second order trapezoidal method is used to numerically integrate the data using the MATLAB embedded *trapz* function.

Numerical simulations of DBD actuators commonly compute the spatial plasma body force, f_{plasma}, which is the force from the plasma discharge acting on the fluid. Typically the plasma force is reported in terms of a *force density*, F_{plasma}, by estimating a volume or in this case an area over which the plasma acts upon. As shown in Equation 2a the x-component of thrust is a combination of the integrated plasma body force and fluidic shear, therefore by estimating the viscous shear the net plasma body force may be recovered. The net shear force, F_{shear}, acting on the plate may be estimated by integrating the viscous shear component, f_{shear}, given by

$$f_{shear} = -\mu \left.\frac{\partial u_x}{\partial y}\right|_{y=y_0} \tag{1}$$

where the dynamic viscosity of air, μ, is taken as 1.86 x 10^{-5} Pa-s. The calculation of the plasma body force enables comparison with predictions from numerical studies.

2. Spatial Body Force Estimation

In the second method, the entire (two-dimensional) flow field is used to estimate the plasma body force. This method has been reported by other groups[15,16]. Compared with the control volume analysis, which only provides integrated quantities, the body force may be computed at all points within the flow field. After applying the aforementioned assumptions (time-averaged, negligible pressure gradient, two-dimensional flow), the incompressible Navier-Stokes momentum equations reduce to

$$f_{plasma,x} = \rho\left(u_x\frac{\partial u_x}{\partial x} + u_y\frac{\partial u_x}{\partial y}\right) - \mu\left(\frac{\partial^2 u_x}{\partial x^2} + \frac{\partial^2 u_x}{\partial y^2}\right), \tag{4a}$$

$$f_{plasma,y} = \rho\left(u_x\frac{\partial u_y}{\partial x} + u_y\frac{\partial u_y}{\partial y}\right) - \mu\left(\frac{\partial^2 u_y}{\partial x^2} + \frac{\partial^2 u_y}{\partial y^2}\right). \tag{4b}$$

where, as mentioned in the previous section, the density of air, ρ, is taken as 1.18 kg/m^3 and the dynamic viscosity of air, μ, is taken as 1.86 x 10^{-5} Pa-s.

Equations 4a and 4b provide the spatial plasma body force distribution over the two-dimensional flow field. The first and second spatial derivatives of the velocity are computed using the built-in MATLAB *gradient* function. The results from this method may be compared to the results of the control volume analysis by integrating the spatial plasma body force over a prescribed area. Figure 15 plots the spatial body force as computed from Equations 4 for a device with 1000 µm ground geometry with a 10-µm-thick silicon dioxide dielectric layer.

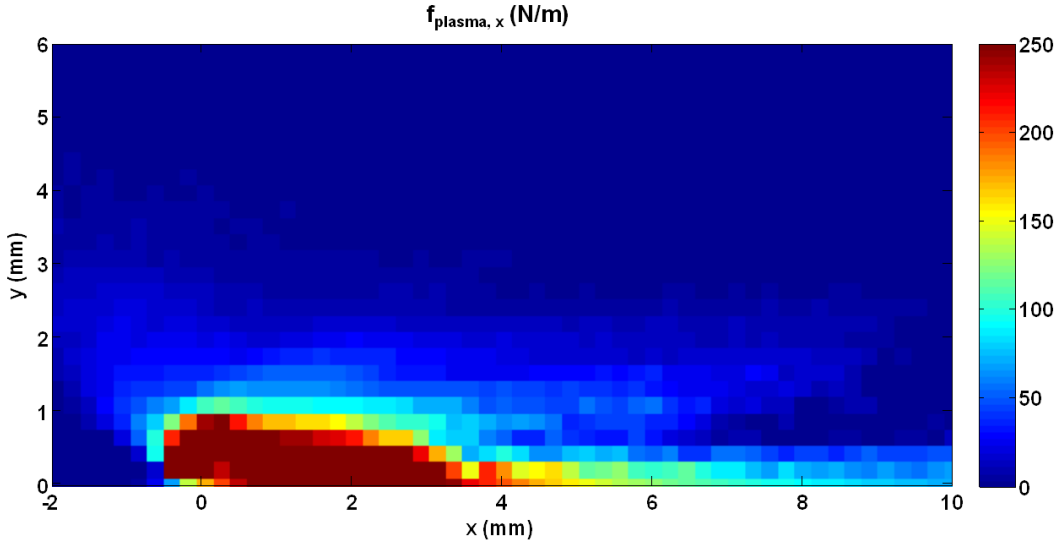

Figure 15. Spatial plasma body force for a microscale DBD actuator with 1000 µm ground geometry and a 10-µm-thick SiO_2 dielectric layer, operated at 7 kVpp and 1 kHz.

3. Investigation of two-dimensional Flow

The assumption that the plasma induced flow is primarily two dimensional is investigated in this section. Two experimental configurations are used in this analysis. First, the actuator is mounted parallel to the laser plane to allow top-view PIV measurements at different heights above the actuator surface. A single-axis manual traverse (Velmex model A-1503-P40-S1.5) allows the floor of the test chamber to translate ± 19 mm. This allows accurate increments in the actuators' location in relation to the laser, which is fixed in position to keep focus with the camera throughout the experiment. Figure 16 shows a top-view velocity contour plot taken just above the surface of the actuator (y = 0.5 mm) for a device with a 1000 µm ground geometry operated at 6 kVpp, 1 kHz. An image of the device is superimposed over the velocity contour to provide the relative location of the DBD actuator with respect to the flow field.

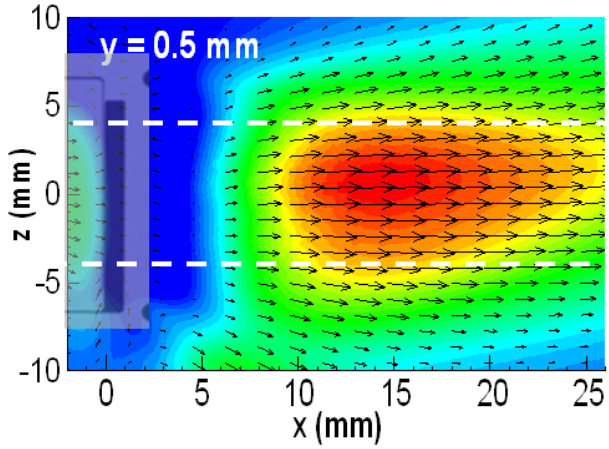

Figure 16. Top view velocity contour, shown with device overlaid to indicate its location relative to the flow field. Displaying x-z plane at y = 0.5 mm for actuator with 1000 µm ground geometry and a 10-µm-thick dielectric layer, operated at 6 kVpp and 1 kHz.

Over the span of the actuator the flow is primarily in the x-direction. Near the edge of the electrodes (z = ±5 mm), the z-component of the velocity becomes significant. However, over the range of z from -4 – 4, corresponding to the spanwise length of the actuator neglecting the edges (indicated with dotted white lines in Fig. 16), the z-component is minimal.

In the second experiment, PIV measurements are taken along the span of the actuator. Starting in the center of the actuator (z = 0 mm), measurements are repeated at z = 2, 4 and 6 mm. Recall the actuator is 10 mm in span, ranging in z from -5 – 5 mm. The data at 0, 2 and 4 mm lie within the plasma generation region, where at z = 6 mm the laser plane is 1 mm past the electrode's length. End effects near the edges of the electrodes are expected to contribute in this region.

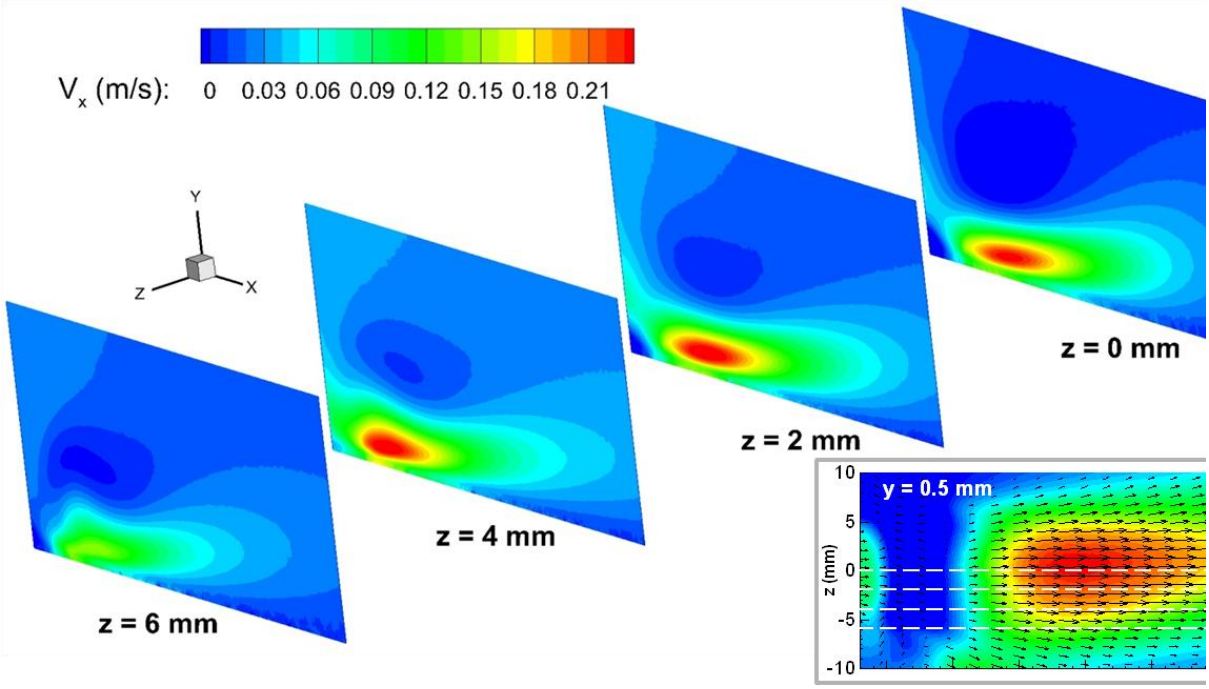

Figure 17. Variation of the velocity field along the span (z-direction) of the microscale actuator. Bottom-right insert shows top-view; dashed lines indicate z-locations of four spanwise velocity contours.

Figure 17 shows the results from the spanwise tests. The insert in the bottom-right indicates the locations corresponding to the four contours shown. The velocity fields show good agreement among the flow from z = 0 – 4 mm. By 6 mm the plane of illumination is beyond the end of the electrodes indicating reduced velocity values at the electrode ends. The top-view velocity contour in addition to these spanwise varying contours provide some justification for the two-dimensional flow assumption.

IV. Results

The results from electrical, fluidic and mechanical measurements are reported in this section.

A. Power Consumption

Average power data is plotted in Fig. 18 for devices with a 5-μm-thick silicon dioxide dielectric layer. The devices are operated at 1 kHz frequency in these tests. The smaller two device geometries (50 μm and 100 μm ground electrodes) show very little consumed power, partly due to their geometry confining the downstream extent of discharge. For these geometries, the devices consume less than 3 W/m of power at 4 kVpp input voltage. For the larger geometry devices (500 μm and 1 mm ground electrodes), significantly more power is consumed, as the plasma region is 5x – 10x larger in area as compared with the small geometries. At 4 kVpp, the largest device dissipated 28 W/m on average, while the device with a 500-μm-wide ground dissipated 15 W/m on average.

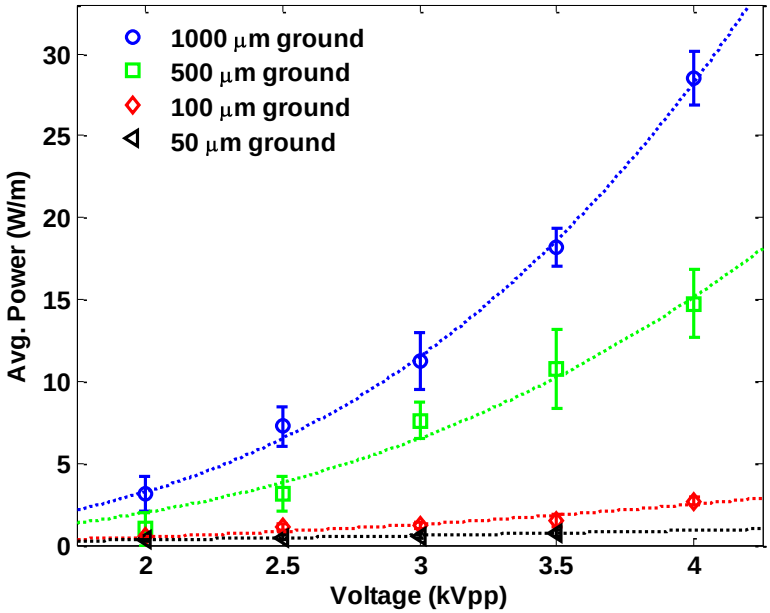

Figure 18. Average power consumed plotted against input voltage for devices with 5-μm-thick silicon dioxide dielectric layer. Four different device geometries are shown.

Figure 19 reports power data for devices with a 10-μm-thick silicon dioxide dielectric layer. At 7 kVpp, the largest device dissipated 41 W/m on average, while the device with a 500-μm-wide ground dissipated 20 W/m on average. At 5 kVpp, the device with 1000 μm ground geometry consumed 19.4 W/m. Compared with the first generation devices with 10-μm-thick polymer dielectric[2], of which the largest similar geometry consumed an average power of 20 W/m at 5 kVpp and 1 kHz, the actuators with silicon dioxide show similar power consumption.

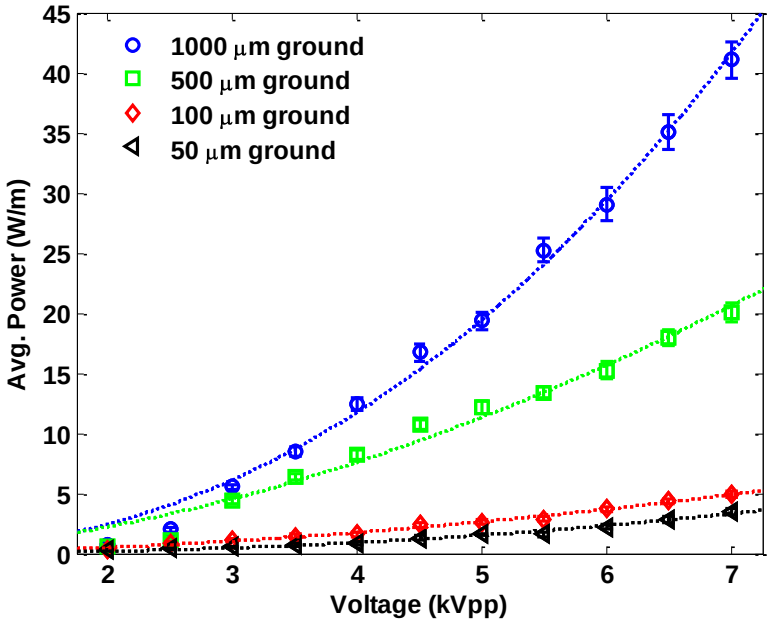

Figure 19. Average power consumed plotted against input voltage for devices with 10-μm-thick silicon dioxide dielectric layer. Four different device geometries are shown.

Comparing the power between the 5 μm and 10 μm silicon dioxide dielectric devices, there is nearly twice the power dissipated from the devices with 5 μm thick SiO_2 at a given input voltage. At 4 kVpp, devices with 10 μm SiO_2 consumed 12.5 W/m as compared to 28.5 W/m consumed for the devices with 5 μm SiO_2. Similarly, the 500

μm geometry device consumed 8.2 W/m and 14.8 W/m at 4 kVpp for the 10-μm and 5-μm-thick dielectrics, respectively. This increase is due to the electric field having larger magnitude across the thinner dielectric. The maximum input voltage is limited by the dielectric strength of the SiO_2 layer. At 1 kHz, the actuators with 5-μm-thick dielectric were able to withstand up to 4 kVpp, while the actuators with 10-μm-thick dielectric could operate up to 7 kVpp.

B. Velocity Data

The velocities induced from the microscale DBD actuators span a range of two orders of magnitude, from less than 0.1 m/s to over 1 m/s. Figures 20 and 21 show velocity profiles for each of the four geometries for devices with 5-μm and 10-μm-thick silicon dioxide dielectric layer, taken at x = 3 mm. These plots illustrate the relative growth in the velocity with increasing input voltage (frequency kept at 1 kHz). Starting with the devices having 5 μm dielectric (Fig. 20), at low voltages (2.0 – 2.5 kVpp range) the plasma is able to induce velocities which are less than 0.1 m/s. Here the fluidic impact is rather weak; instead of a downstream directed wall jet, the plasma is only able to very locally interact with the fluid. The flow filed in this case shows a small downstream effect; just downstream from the plasma region the fluid is no longer attached to the wall but instead begins to separate from the wall and recirculate above the actuator surface. With increasing voltage the plasma region is able to impart more momentum into the fluid, creating the characteristic wall jet that is similar to the macroscale actuators. Increasing the input voltage provides a corresponding increase in the induced wall jet velocity, with larger device geometries inducing greater velocities.

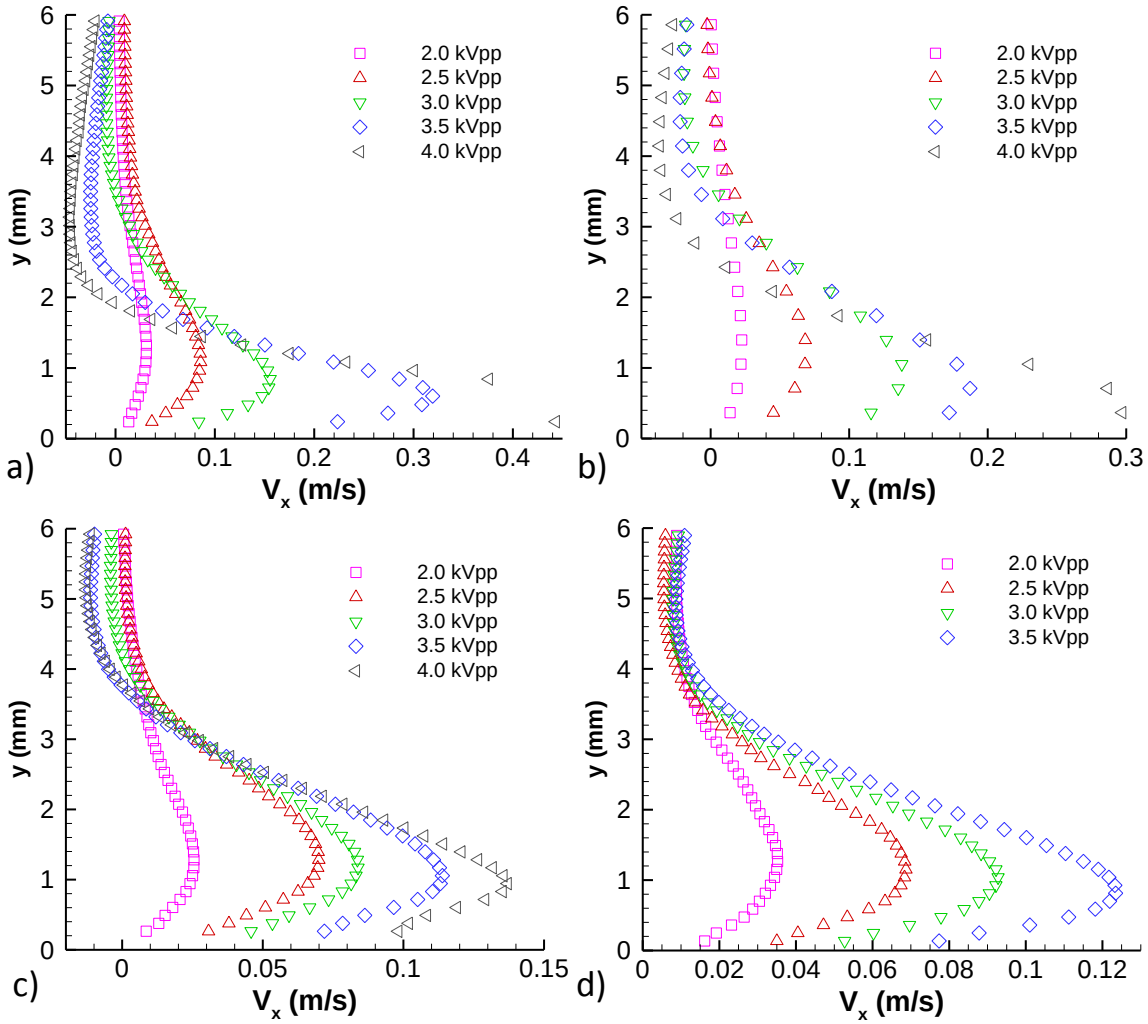

Figure 20. Velocity profiles of four microscale DBD actuator geometries having a 5-μm-thick dielectric layer, taken at x = 3mm downstream. a) 1000 μm wide ground electrode, b) 500 μm ground, c) 100 μm ground, and d) 50 μm ground. Voltage varies from 2 – 4 kVpp, at 1 kHz frequency.

Comparing similar geometries but different dielectric thickness, the induced velocities are in close agreement. At 4 kVpp, the 1000 µm ground geometry shows 0.45 m/s for both dielectrics. Similar agreement is indicated for devices with 500 µm and 100 µm geometries, with slightly higher velocity produced for the device with the 5-µm-thick dielectric. The actuator with a 1-mm-wide ground electrode creates velocities up to 1.5 m/s when operated at 7 kVpp for the 10 µm dielectric case (Fig. 21). While the smallest device, having a 50-µm-wide ground, shows a maximum velocity as low as 0.04 m/s when operated at 2 kVpp, and reaches up to 0.41 m/s at 7 kVpp. The geometry, specifically the width of the ground electrode, governs the extent of the plasma discharge region. Larger actuators provide greater regions of discharge which in-turn are able to impart more momentum into the surrounding fluid.

The thickness of the wall jet can also be inferred from the velocity profile data. The geometry of the DBD actuator affects the height of the fluid jet as well as the velocity, but to a lesser extent. The wall jet thickness is generally around 2 mm, but varies up to ~3 mm for smaller geometries at lower input voltages. The larger devices, providing the strongest momentum coupling between the plasma discharge and surrounding air, create thinner and longer wall jet regions as compared with smaller device geometries.

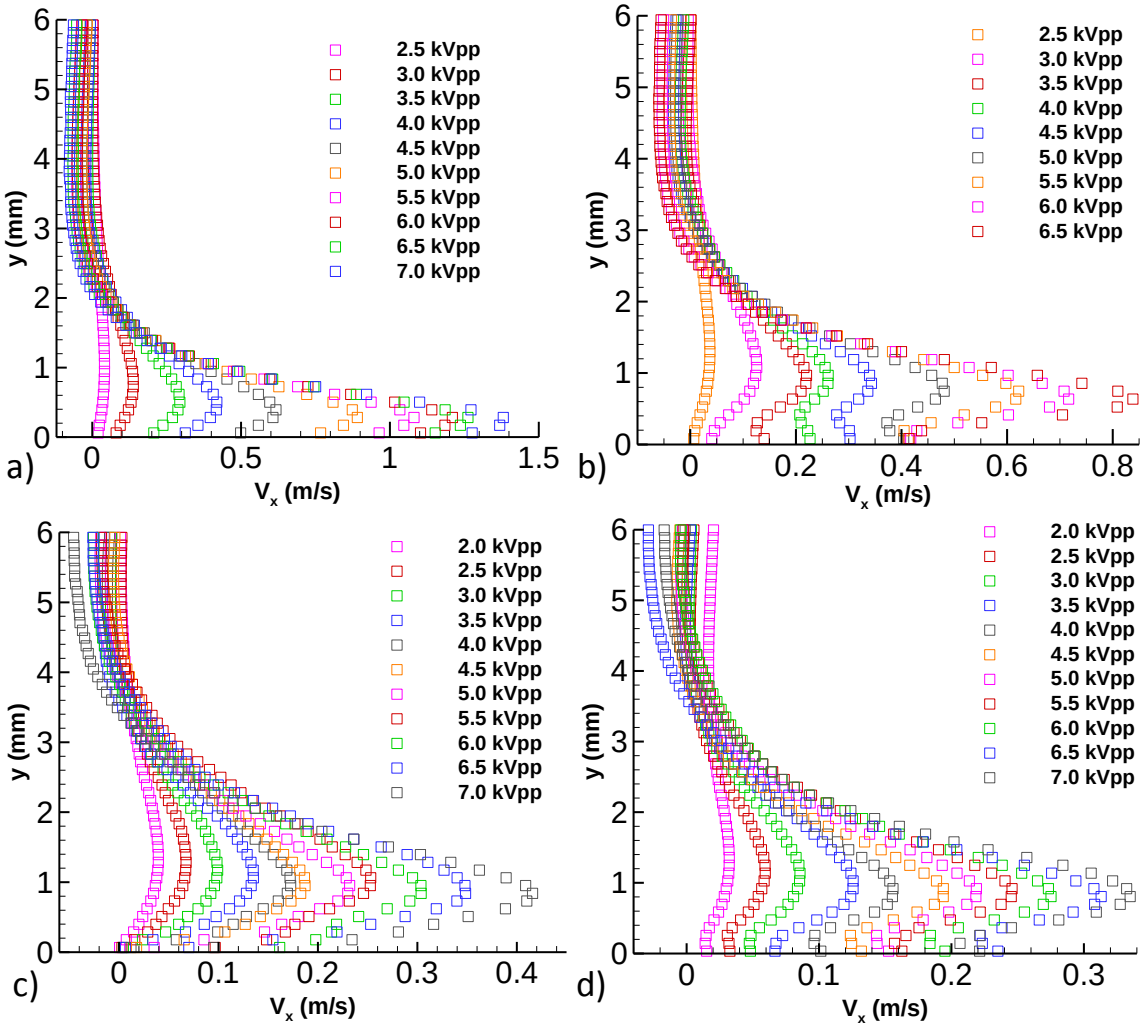

Figure 21. Velocity profiles of four microscale DBD actuator geometries having a 10-µm-thick dielectric layer, taken at x = 3mm downstream. a) 1000 µm wide ground electrode, b) 500 µm ground, c) 100 µm ground, and d) 50 µm ground. Voltage varies from 2 – 7 kVpp, at 1 kHz frequency.

Another useful way to plot the velocity data is to plot the absolute maximum x-component of velocity as shown in Fig. 22. This is similar to looking at the maximum velocity from each of the velocity profile plots in Figs. 20 and 21 (above), but accounts for all x locations while the velocity profiles are extracted at a specific downstream location (x = 3 mm). It also provides a clear visual interpretation of the max velocity trend with voltage.

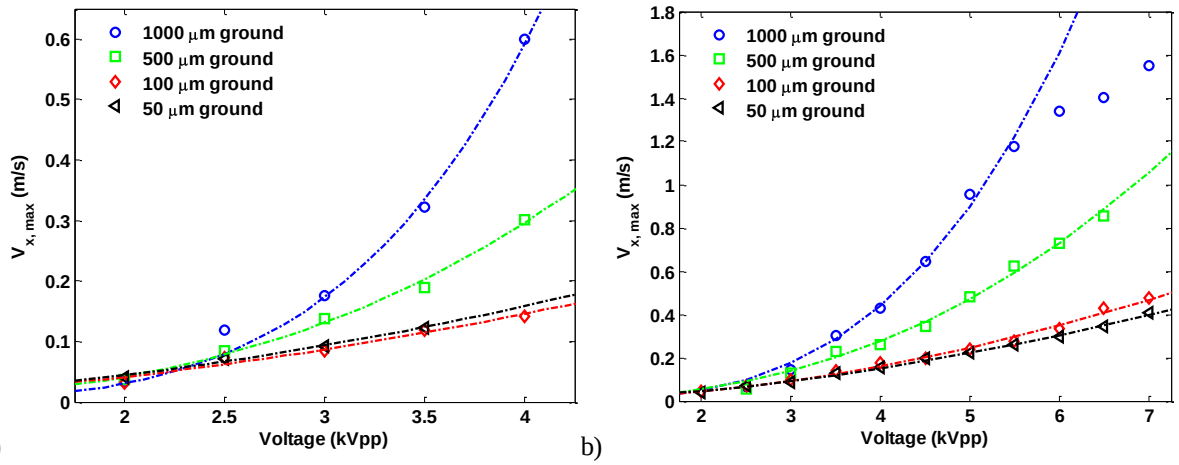

Figure 22. Plot of maximum velocity (x-component)as a function of voltage input for various microscale DBD actuator geometries. a) Devices with 5-µm-thick SiO_2, b) devices with 10-µm–thick SiO_2 dielectric.

A third way to analyze the velocity data is to plot the entire flow field. Figure 23 plots velocity contours of two device geometries for voltages ranging from 3 – 7 kVpp at 1 kHz frequency. The left column corresponds to a device with a 100 µm ground electrode and the right column for a device with a 1000 µm ground, and both having 10-µm-thick dielectric barriers. Starting with the larger geometry shown in the right column, with increasing voltage the induced wall jet becomes thinner and has more downstream effect. From 2.5 to about 4 kVpp, the induced velocity is fairly weak (< 1 m/s) and the flow begins to dissipate away from the wall by ~ 10 mm downstream. For these voltages, the y-location of the max velocity value is above 1 mm from the surface. At voltages of 4.5 kVpp and above, the induced velocity resembles the characteristic wall jet produced by macroscale actuators. The location of the max velocity value is consistently at y = 0.86 mm, and varies in x-location from 1.5 – 1.7 mm, occurring just past the downstream extent of the discharge. The velocity reaches ≥1 m/s when the voltage is ≥ 5 kVpp for this device geometry.

In the left column of Fig. 23, for the device with a 100 µm wide ground electrode, the induced velocities reach 0.48 m/s at 7 kVpp, and just 0.05 m/s at 2 kVpp. From 2 – 4 kVpp the induced velocity begins to dissipate by ~ 10 mm downstream, similar to the larger geometry. Between 4 – 5 kVpp the velocity transitions into a wall jet with a more narrow and traditional profile. For these voltages, the y-location of the max velocity is between 1.4 – 1.6 mm, and the x-location of the max velocity is pushed further downstream, between 5 – 6.5 mm. Even though the velocity values are relatively small, they're fluidic effect extends over 25 mm downstream. The total width of the device geometry in the streamwise direction is only 0.25 mm (top electrode width, gap, and ground electrode width); showing that the reduced size actuator can have significant downstream fluid effects, especially for its size.

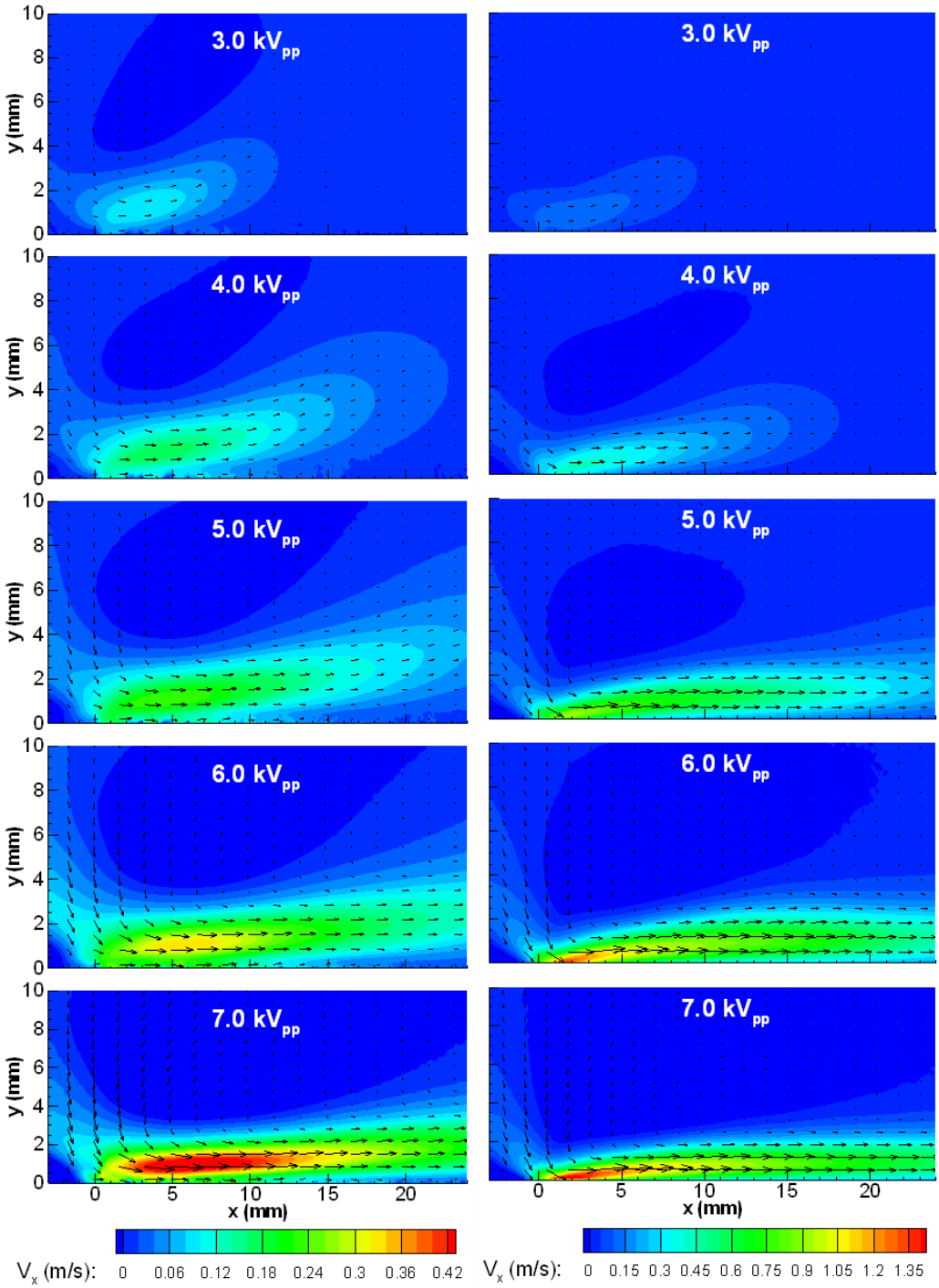

Figure 23. Velocity contour plots for microscale DBD actuator having 1000 µm ground (left column) and 1000 µm ground (right column). For clarity, the contours have independent scaling as indicated below each column.

The dependence of the induced velocity on the input frequency was also investigated. The device tested in this experiment had 100 µm ground geometry and a 10-µm-thick silicon dioxide dielectric layer. The input voltage was held constant at 4 kVpp while the frequency was varied from 100 Hz up to 20 kHz. This range covers two orders of magnitude for the applied frequency, which corresponds to the range of frequencies that are possible with our lab equipment.

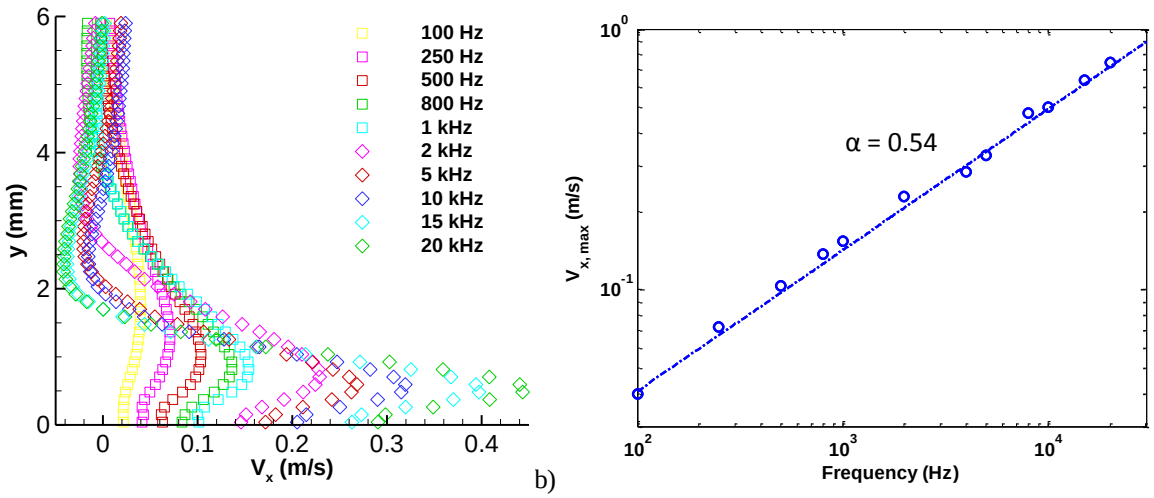

a) b)

Figure 24. a) Velocity profiles plotted against frequency, taken at x = 3 mm downstream; device input voltage held constant at 4.0 kVpp; b) Maximum x-component of velocity for various frequencies, plotted with logarithmic axes.

The velocity profiles are plotted in Fig. 24a for the range of frequencies from 100 Hz to 20 kHz. The results are similar in trend with that observed from varying the voltage input: with higher frequency there is greater induced velocity, but to a lesser extent. Figure 24b plots the maximum induced velocity as a function of the input frequency. Both axes are plotted in logarithmic scale; here, the slope of the fit line (α = 0.54) indicates the power law relationship between the induced velocity and signal frequency.

C. Thrust/Force Data

In this section, data is reported for the extracted thrusts and net plasma body forces. Starting with the thinner dielectric case, the x- and y-components of the thrust are plotted in Fig. 25 for devices with 5 µm SiO_2. These devices indicate streamwise (x-component) thrust values up to 0.20 mN/m and wall normal (y-component) values reaching just 0.05 mN/m. The streamwise thrust component is on average about four times that of the wall normal component. The actuators with 50 and 100 µm ground electrodes show similar thrust values for both x- and y-components. For these two geometries, the downstream extent of the plasma is 150 µm and 200 µm, respectively (including the 100 µm gap between electrodes as well as the ground electrode width). There is little difference in the induced velocities and thrust forces for these geometries.

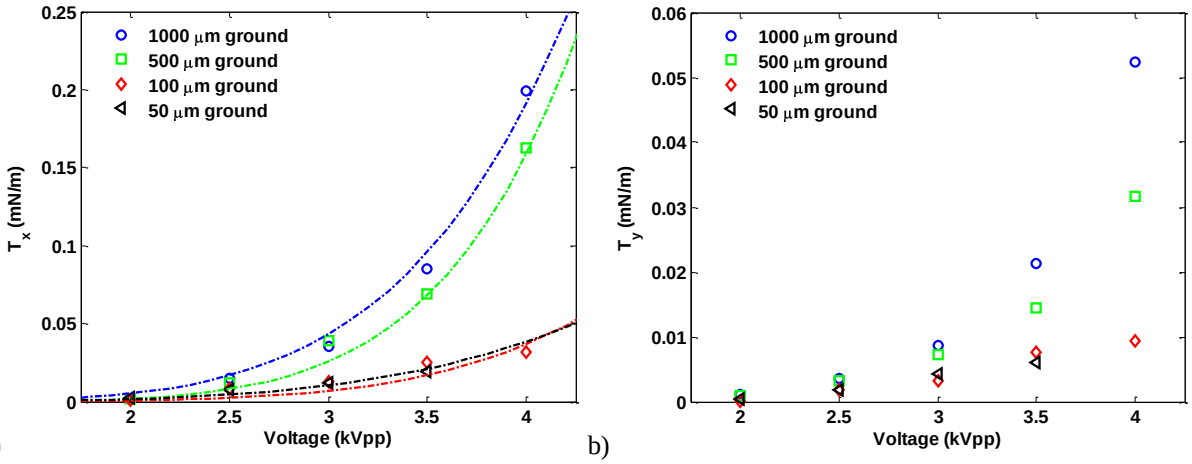

a) b)

Figure 25. Thrust values computed based on the control volume analysis for devices with 5 µm SiO_2 dielectric; a) x-component, and b) y-component.

The net plasma force acting on the fluid is shown in Fig. 26. This data is computed by integrating the spatial body force at all points within the two-dimensional flow field. The streamwise plasma force reaches 0.35 mN/m while the y-component reaches 0.05 mN/m. The y-components of the plasma force match fairly well with the y-

component from the thrust data. In contrast, the plasma force shows significantly larger values for the x-component as compared with the thrust. The difference in these values is due to the loss of momentum along the actuator's surface.

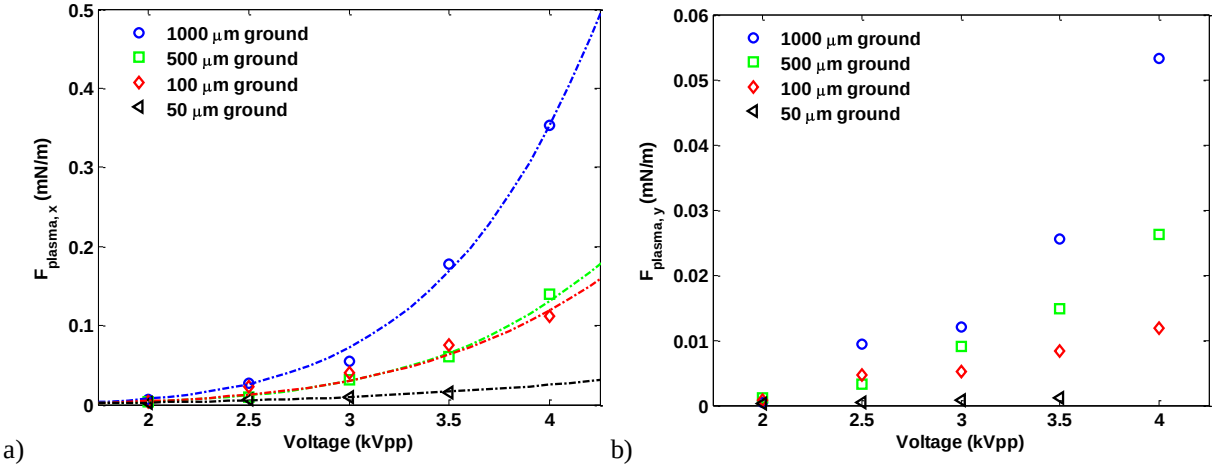

Figure 26. Plasma force computed from the spatial body force estimation for devices with 5 μm SiO_2 dielectric; a) x-component, and b) y-component.

Similar results are reported next for the devices having a 10-μm-thick SiO_2 dielectric barrier (Fig. 27). Thrust values reach 1.4 mN/m for the streamwise direction and 0.3 mN/m in the wall-normal direction for the largest device geometry. These devices are able to sustain plasma at higher voltages compared with the devices having a thinner dielectric layer, enabling higher forces to be achieved due to the power law relationship of the thrust upon the input voltage.

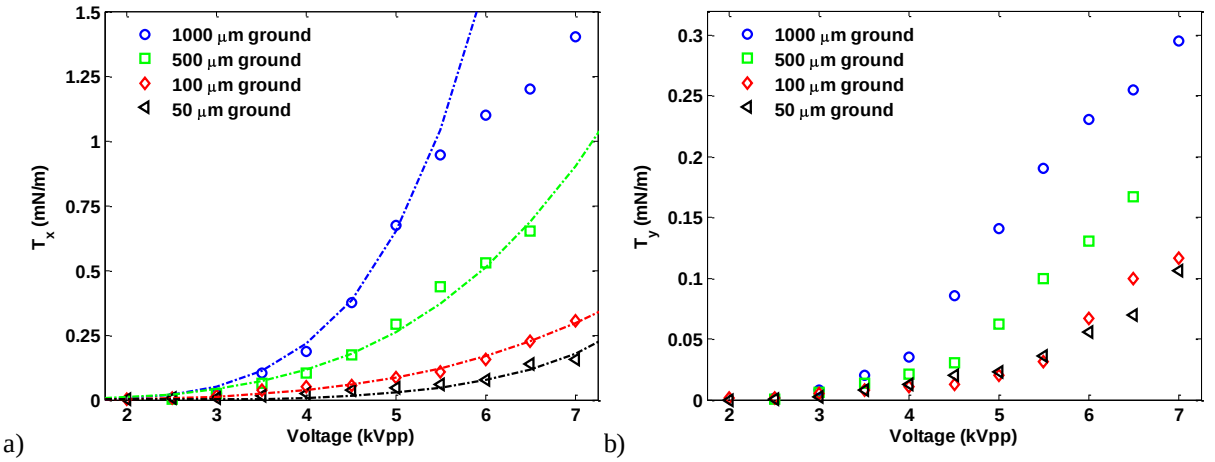

Figure 27. Thrust values computed based on the control volume analysis for devices with 10 μm SiO_2 dielectric; a) x-component, and b) y-component.

The plasma force is also plotted for the devices having 10 μm SiO_2 in Fig. 28. Here, the plasma force reaches 2.3 mN/m for the largest actuator geometry at 7 kVpp. The device having 50 μm ground geometry produces a plasma force of 0.22 mN/m at 7 kVpp, indicating a range of force values spanning an order of magnitude. The wall-normal or y-component of the plasma force reaches up to 0.13 mN/m, and as low as 0.05 mN/m at 7 kVpp.

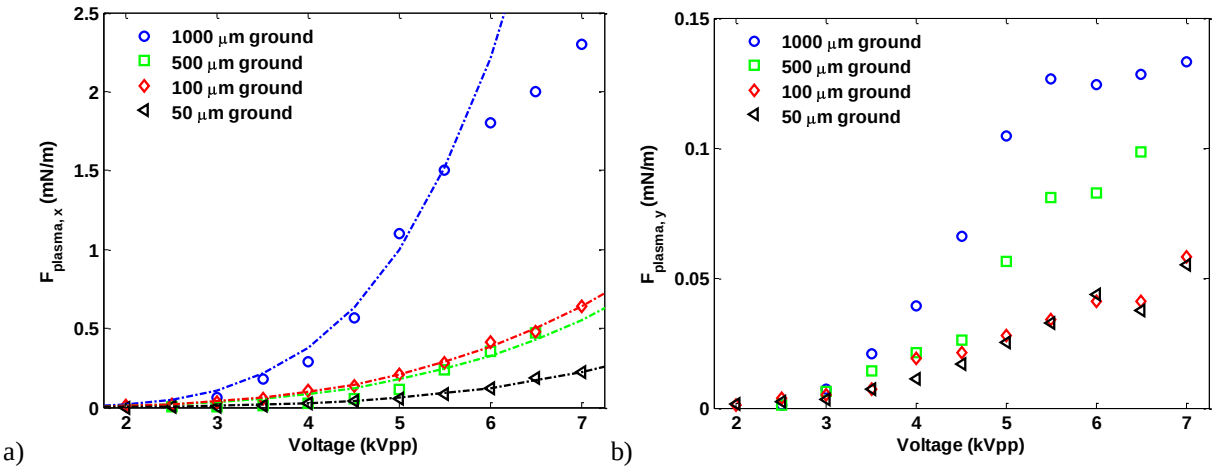

a) b)

Figure 28. Plasma force computed from the spatial body force estimation for devices with 10 μm SiO_2 dielectric; a) x-component, and b) y-component.

Similar to the data from the actutaors with 5-μm-thick dielectric, the plasma force values are consistently larger than the thrust values. Recall from Equations 3, the shear force may be estimated by integrating the viscous shear component. Adding the net shear force to the thurst enables a method to estimate the plasma body force. Figure 29 plots the plasma force from integrating the spatial body force for comparison with the thurst while including the additional shear force. There is reasonble agreement between these two methods of computing the plasma force. Two of the four actuator geometries are shown for clarity (1000 μm and 100 μm ground electrodes) for the two dielectric thicknesses investigated. The device with 100 μm geometry shows nearly equal values between the two methods, while the values vary more for the larger geometry.

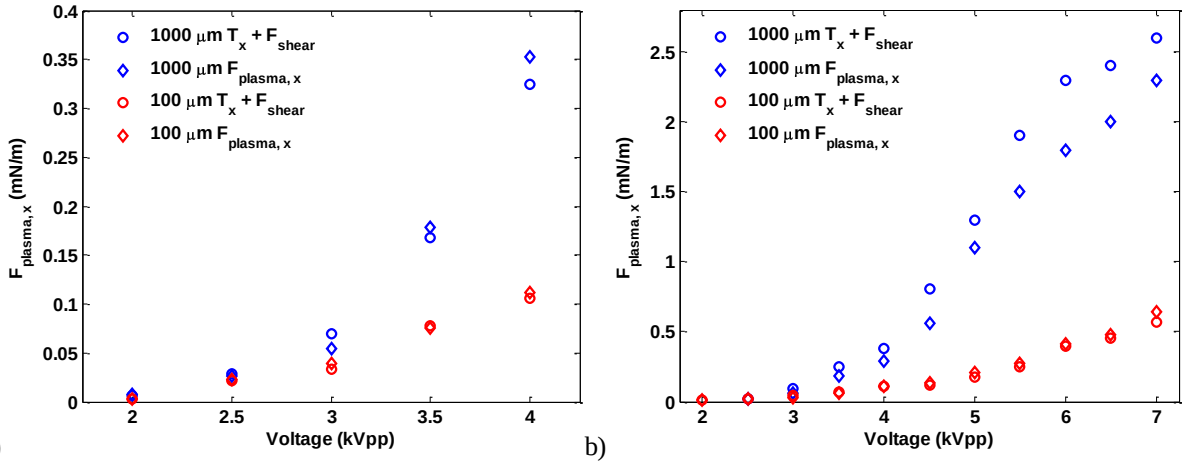

a) b)

Figure 29. Comparison between control volume estimation and direct integration of spatial body force for devices with a) 5 μm SiO_2 and b) 10 μm SiO_2.

Thrust values are plotted in Fig. 30 for the range of frequencies investigated for the device with 100 μm ground geometry and a 10-μm-thick dielectric layer. At 100 Hz the parallel thrust value indicates 0.005 mN/m as the maximum velocity at this electrical input (4 kVpp, 100 Hz) reaches just 0.04 m/s. At 1 kHz, the thrust computed is 0.05 mN/m and by 20 kHz the thrust reaches 0.50 mN/m. Here the frequency and corresponding thrust values both cover two orders of magnitude. The trend of increasing thrust with frequency is apparent from these plots, however the dependency of both velocity and force values are largest with respect to increasing input voltage.

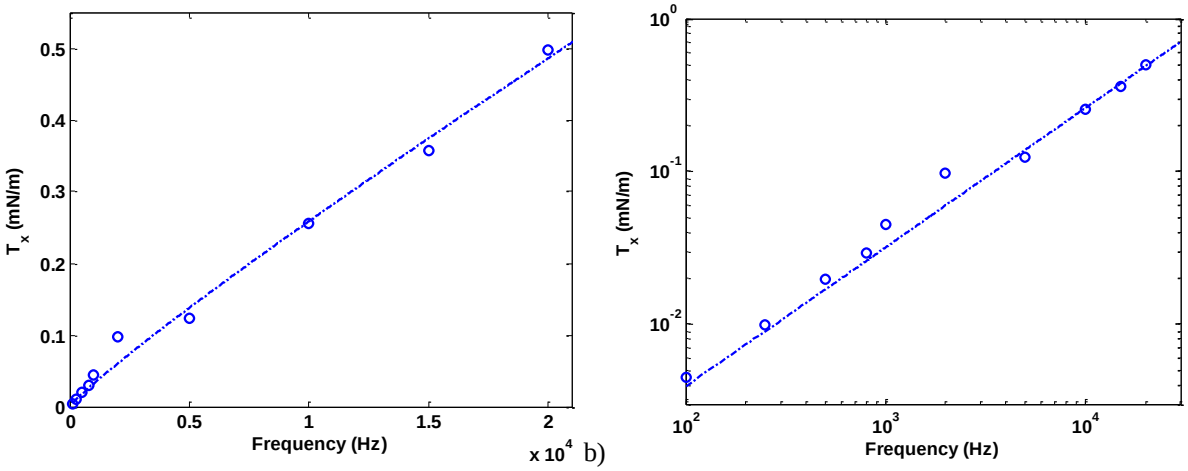

Figure 30. Streamwise thrust component plotted against frequency for devices with 100 µm ground geometry and 10 µm SiO_2 dielectric, operated at 4.0 kVpp. a) Linear scale, b) log scale.

V. Conclusion

In summary, four geometries of microscale DBD actuators were fabricated with 5- and 10-µm-thick silicon dioxide for the dielectric barrier. The average power ranges from less than 1 W/m at 2 kVpp to 41 W/m at 7 kVpp for the largest actuator geometry, and up to just 3 W/m for the smallest geometry. The microscale actuators are able to induce a wall jet with velocity up to 1.5 m/s. The wall jet extends over 25 mm downstream, produced from a plasma region that extends just 1.1 mm in the streamwise direction. The smallest actuators (50 µm ground geometry) show velocities as low as 0.04 m/s and only locally interact with the fluid. The flow separates from the actuator's surface and has little downstream effect, perhaps lending itself to applications requiring periodic flow interactions with high spatial resolution.

The thrust force is reported as computed using the control volume analysis, and the plasma force is integrated over the spatial body force estimate. Thrust values reach 1.4 mN/m, while the plasma body force reaches up to 2.3 mN/m. The net shear force is approximated and added to the thrust in order to recover the total force and compare with the plasma body force values. The combined thrust and shear forces provide 2.6 mN/m, close in agreement with the plasma body force (2.3 mN/m). Good agreement was observed between the two forces based on these methods over the range of voltages tested for the different actuator geometries.

The power, induced velocities, and plasma force data also span about an order of magnitude between device geometries over most voltages tested, indicating that the geometry can be utilized as a control variable to limit the power which in turn limits the output performance for a given input voltage and frequency.

Using SiO_2 for the dielectric barrier increased the lifetime of the actuators compared with the first generation of DBD actuators which utilized a polymer dielectric material. The average consumed power shows similar agreement (comparing equal dielectric thickness) between the SiO_2 and polymer based devices[2]. However, slightly lower induced velocities are observed for the silicon dioxide actuators: 1.5 m/s compared with 2.0 m/s for the device with 1000 µm ground geometry. Similarly, the parallel thrust component reaches 1.4 mN/m for devices with SiO_2 and 3.0 mN/m for the devices with polymer dielectric. The increased device reliability gained from using a ceramic dielectric indicates a trade-off with device performance.

Acknowledgments

This work was supported in part by AFOSR Grant # FA9550-09-1-0416 and ARO Grant # W911NF-09-1-0511. The authors would also like to thank the staff of the UF Nanoscale Research Facility for their assistance in the fabrication processes.

References

[1]Kogelschatz, U., "Dielectric-Barrier Discharges: Their History, Discharge Physics, and Industrial Applications", *Plasma Chemistry and Plasma Processing*, Vol. 23, 1 (2003).

[2]Zito, J. C., Durscher, R. J., Soni, J., Roy, S., and Arnold, D. P., "Flow and Force Inducement Using Micron Size Dielectric Barrier Discharge Actuators," *Appl. Phys. Lett.*, Vol. 100, 193502, 2012.

[3]Pons, J., Moreau, E., and Touchard, G., "Asymmetric Surface Dielectric Barrier Discharge in Air at Atmospheric Pressure: Electrical Properties and Induced Airflow Characteristics", *J. Phys. D: Appl. Phys.*, Vol. 38, 3635-3642 (2005).

[4]Hoskinson, A. R., Hershkowitz, N., and Ashpis, D. E., "Force Measurements of Single and Double Barrier DBD Plasma Actuators in Quiescent Air", *J. Phys. D: Appl. Phys.*, Vol. 41, 245209 (2008).

[5]Hoskinson, A. R., and Hershkowitz N., "Differences between Dielectric Barrier Discharge Plasma Actuators with Cylindrical and Rectangular Exposed Electrodes", *J. Phys. D: Appl. Phys.*, Vol. 43, 065205 (2010).

[6]Kriegseis, J., Grundmann, S., and Tropea, C., "Progress Toward Accurate Measurements of Power Consumptions of DBD Plasma Actuators", *50th AIAA Aerospace Sciences Meeting*, Nashville, TN, Jan. 9-12, 2011.

[7]Ashpis, D. E., Laun, M. C., and Griebeler, E. L., "Power Consumption, Discharge Capacitance and Light Emission Measurements for Thrust Production of Dielectric Barrier Discharge Plasma Actuators", *J. Appl. Phys.*, Vol. 110, 013305 (2011).

[8]Kriegseis, J., Schroter, D., Barckmann, K., Duchmann, A., Tropea, C., and Grundmann, S., "Closed-Loop Performance Control of Dielectric-Barrier-Discharge Plasma Actuators", *J. AIAA*, Vol. 51, 4 (2013).

[9]Durscher, R., and Roy, S., "Evaluation of Thrust Measurement Techniques for Dielectric Barrier Discharge Actuators", *Exp. Fluids*, Vol. 53, 1165-1176 (2012).

[10]TSI Model 9302 Atomizer, Instruction Manual, TSI, September, 2000.

[11]Gregory, J. W., Enloe, C. L., Font, G. I., and McLaughlin, T. E., "Force Production Mechanisms of a Dielectric-Barrier Discharge Plasma Actuator", *45th AIAA Aerospace Sciences Meeting*, Reno, NV, Jan. 8-11, 2007.

[12]Enloe, C. L., McHarg, M. G., and McLaughlin, T. E., "Time-Correlated Force Production Measurements of the Dielectric Barrier Discharge Plasma Aerodynamic Actuator", *J. Appl. Phys.*, Vol. 103, 073302 (2008).

[13]Enloe, C. L., McHarg, M. G., Font, G. I., and McLaughlin, T. E., "Plasma-Induced Force and Self-Induced Drag in the Dielectric Barrier Discharge Aerodynamic Plasma Actutaor",*47th AIAA Aerospace Sciences Meeting*, Orlando, FL, Jan. 5-8, 2009.

[14]Font, G. I., and McLaughlin, T. E., "Plasma Volumetric Effects on the Force Production of a Plasma Actuator", *J. AIAA*, Vol. 48, 9 (2010).

[15]Kotsonis, M., Ghaemi, S., Veldhuis, L., and Scarano, F., "Measurement of the Body Force Field of Plasma Actuators", *J. Phys. D: Appl. Phys.*, Vol. 44, 045204 (2011).

[16]Kriegseis, J., Schwarz, C., Tropea, C., and Grundmann, S., "Velocity-Information-Based Force-Term Estimation of Dielectric Barrier Discharge Plasma Actuators", *J. Phys. D: Appl. Phys.*, Vol. 46, 055202 (2013).

[17]Neumann, M., Friedrich, C., Czarske, J., Kriegseis, J., and Grundmann, S., "Determination of the Phase-Resolved Body Force Produced by a Dielectric Barrier Discharge Plasma Actuator", *J. Phys. D: Appl. Phys.*, Vol. 46, 042001 (2013).

[18]Enloe, C. L., McLaughlin, T. E., Font, G. I., and Baughn, J. W., "Parameterization of Temporal Structure in the Single-Dielectric-Barrier Aerodynamic Plasma Actuator", *J. AIAA*, Vol. 44, 6 (2006).